

Investigating the time dependence of neutron-proton equilibration using molecular dynamics simulations

A. Jedele,^{1,2,*} K. Hagel¹, M. Q. Sorensen^{1,2}, B. Harvey^{1,3}, A. Abbott,^{1,2} J. Gauthier,¹ A. Hannaman^{1,2}, A. A. Hood,¹ Y.-W. Lui,¹ L. McCann,^{1,2} A. B. McIntosh,¹ L. A. McIntosh,¹ S. Schultz^{1,2}, Z. Tobin,^{1,2} R. Wada,¹ M. Youngs,¹ and S. Yennello^{1,2,3}

¹Cyclotron Institute, Texas A&M University, College Station, Texas 77840, USA

²Chemistry Department, Texas A&M University, College Station, Texas 77840, USA

³Physics Department, Texas A&M University, College Station, Texas 77840, USA



(Received 10 August 2022; accepted 3 January 2023; published 1 February 2023)

Neutron-proton equilibration has previously been studied experimentally in dynamically deformed nuclei in heavy ion collisions [Phys. Rev. Lett. **118**, 062501 (2017); Phys. Rev. C **95**, 044604 (2017)] using the NIMROD detector array at the Cyclotron Institute at Texas A&M University. Results indicated the composition of the two heaviest fragments originating from the excited projectile-like fragment evolved exponential with respect to their orientation angle to be more similar. Constrained Molecular Dynamics and Antisymmetrized Molecular Dynamics simulations were performed for different formulations of the density dependence of the asymmetry energy term of the nuclear equation of state. The simulations are compared to experimental results, which indicate a better agreement with a softer interaction in the nuclear equation of state.

DOI: [10.1103/PhysRevC.107.024601](https://doi.org/10.1103/PhysRevC.107.024601)

I. INTRODUCTION

The nuclear equation of state (nEoS) has a broad impact on terrestrial and astrophysical phenomena such as isotopic abundances, cluster formation at low densities, outer crust of neutron stars, and heavy element formation in supernova explosions [1]. Of particular importance is constraining the density dependence of the asymmetry energy term [$E_{\text{sym}}(\rho)$]. The asymmetry energy corresponds to the difference in binding energy between pure neutron matter and symmetric nuclear matter ($N = Z$). The constraints in the density dependence of the asymmetry term are usually reported in terms of the saturation energy [$S_0 = E_{\text{sym}}(\rho_0)$] and slope of the asymmetry energy at saturation density [$L = 3\rho_0 \frac{\partial E_{\text{sym}}(\rho)}{\partial \rho} |_{\rho_0}$]. While the value of S_0 is reasonably well constrained [1,2], the value of L is still poorly constrained. This leads to a range of functional forms for the density dependence of the asymmetry energy.

In the laboratory, heavy-ion collisions can give insight into the density dependence of the nEoS. This analysis focuses on the neutron-proton (NZ) equilibration. In the momentum dampening phase of the projectile and target interaction, a low-density neck region is formed between the two fragments, allowing for neutron and proton flow. The neck region is characterized as being relatively neutron rich due to a lower value of the asymmetry energy [3]. The extent of the neutron and proton flow is governed by the form of the density dependence of the nEoS. Due to the velocity gradient, the interacting

projectile and target become highly elongated before breaking apart into an excited projectile-like fragment (PLF*) and an excited target-like fragment (TLF*). Focus has been given to the dynamics of the PLF* due to limitations in detecting the TLF*. The collisions of a peripheral and midperipheral nature cause the PLF* to rotate around its center of mass before breaking apart into a heaviest fragment (HF) and second heaviest fragment (LF).

The PLF* decays via two mechanisms: Statistical and dynamical. For dynamical decay, the PLF* is highly deformed and elongated causing it to break apart on a very short timescale of approximately 10^{-21} s or 300 fm/c. The fragments break apart along the PLF-TLF axis of separation and generally in order of size with the HF decaying forward of the LF [4–6]. In the case of statistical decay, surface tension is strong enough to prevent dynamical decay resulting in a spherical PLF*. This will then decay isotropically on a longer timescale ($\approx 10^{-20}$ – 10^{-19} s).

Because the regions from which the HF and LF originate have a different chemical potential, neutrons and protons are exchanged to minimize this difference, a process which is referred to as neutron-proton (NZ) equilibration. For dynamical decay, the contact time between the HF and LF is short, minimizing the extent of the NZ equilibration. Therefore, the LF is more neutron-rich in comparison to the HF, which is more neutron-poor [3–5,7]. In the case of statistical decay, the fragments achieve equilibrium before breaking apart.

Previous experimental results [8,9] showed the evolution of the NZ equilibration to be exponential for both the HF and LF with an average mean equilibration time of 0.3 zs or 10^{-21} s (≈ 100 fm/c). While the results give insight into the dynamics of the NZ equilibration, comparison to simulations

*Present address: Institut für Kernphysik, TU-Darmstadt, Darmstadt 64289, Germany; a.jedele@gsi.de

can give further insight into the functional form of the density dependence of the nEoS.

II. EXPERIMENTAL AND SIMULATION PARAMETERS

The experimental results were obtained at the Cyclotron Institute at Texas A&M University using the K500 Superconducting cyclotron. The $^{70}\text{Zn} + ^{70}\text{Zn}$ reaction was performed using the Neutron Ion Multidetector for Reaction Induced Dynamics (NIMROD) [10]. NIMROD was chosen due to its large angular coverage ranging from 3.6° to 167.0° , and excellent isotopic resolution up to $Z = 17$ in many detectors and $Z = 20$ in select Si-Si-CsI stacks [11]. Elemental resolution was achieved up through the beam ($Z = 30$). The combination of the angular coverage and the isotopic resolution was key to measuring the neutron-proton equilibration with high resolution.

Constrained Molecular Dynamics (COMD) [12] and Antisymmetrized Molecular Dynamics (AMD) [13] are molecular dynamics codes, which simulate the collision dynamics by solving time-dependant wave functions. AMD maintains the Pauli exclusion principle by solving antisymmetrized Slater determinants, and COMD maintains the Pauli exclusion principle using occupational densities. A Skyrme interaction was used for the parametrization of the density dependence of the nEoS.

For the COMD simulations, 10^7 events were simulated for each asymmetry energy parameter. The simulation used a triangular impact parameter distribution and stopped at 1000 fm/c, at which point the vast majority of the dynamical decays have occurred [14]. The same energy corresponding to the saturation density was used [$E_{\text{sym}}(\rho_0) = 30$ MeV]. The slopes extracted from the input parameters correspond to $L = 51$ MeV for the soft interaction, $L = 75$ MeV for the stiff interaction and $L = 105$ MeV for the superstiff interaction.

For the AMD simulations, 10^5 events were simulated for each asymmetry energy parameter using a combination of uniform and triangular distributions (5% and 95%, respectively, for the soft interaction, and 8% and 92%, respectively, for the stiff interaction). The simulations were stopped at 300 fm/c due to the significant CPU time required. For the density dependence of the asymmetry energy, two parametrizations were used. The energy at saturation density was $E_{\text{sym}}(\rho_0) = 30.5$ MeV for both interactions. The L values selected were $L = 21$ MeV for the soft interaction and $L = 65$ MeV for the stiff interaction.

Two approaches were taken to analyze the neutron-proton equilibration results. In the first case, the fragments at the end of the COMD or AMD simulation were passed through a software filter replicating the experimental conditions. In the second case, the fragments at the end of the COMD or AMD simulations were further de-excited using the GEMINI de-excitation code [15] before being filtered. Figure 1 shows the normalized total charge and mass distributions for the experimental data plotted in black, COMD data plotted in teal, and AMD data plotted in purple. The solid lines correspond to the results without GEMINI de-excitation. All distributions are normalized by the total yield. The jagged nature of the experimental mass distribution is due to isotopic identification

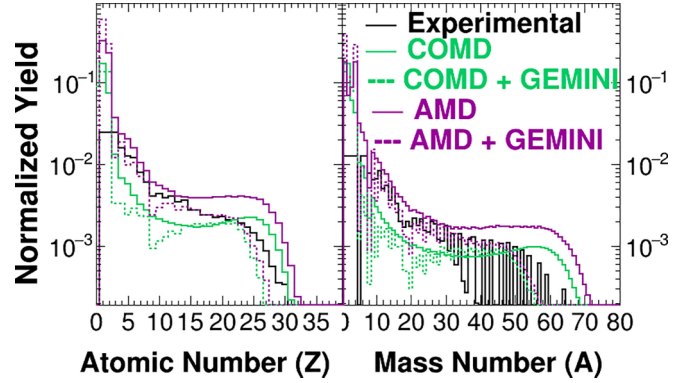


FIG. 1. Experimental and simulated charge distributions (left) and mass distribution (right) of all particles that were detected in NIMROD or passed the software replica filter. The black lines represent the experimental distributions. The solid lines are the results without GEMINI and the dotted lines are results after GEMINI is applied. The teal lines correspond to the COMD results and the purple lines correspond to the AMD results. The simulated charge distributions reproduce the experimental results well. The simulated mass distributions slightly overproduce the total mass of the system. The jagged nature of the experimental results is due to the isotopic identification of the heaviest fragment.

of the fragments with a charge of $Z \geq 17$. In the NIMROD array, charge identification is achieved up through the beam. However, the mass resolution was only achieved up through $Z = 17$ in many Si-Si-CsI stacks and up through $Z = 21$ in one stack. For the fragments without mass resolution, the fragment was assigned a *GuessA* value equal to the most common isotope for each atomic number. Overall, the simulations reproduce the elemental and mass distributions well with better agreement observed for the simulations after the GEMINI de-excitation code was applied.

III. DETERMINING THE SOURCE

In order to focus on the dynamical decay of the PLF*, events were selected in which at least two heavy charged particles were identified after being passed through the experimental filter. The fragments were sorted by atomic number followed by mass number for charge-equivalent particles. The heavier of the two fragments was labeled the **HF**, or heavy fragment, and required to have an atomic number of at least $Z_H \geq 12$. The second heaviest fragment was labeled the **LF**, or light fragment, and required to have a charge of at least $Z_L \geq 3$. In the experimental data, both fragments were required to be isotopically identified. All simulated data were isotopically identified. A total charge requirement of $21 \leq Z_{\text{tot}} \leq 32$ was also implemented, which included the Z_H , Z_L and all other charged particles that passed through the filter.

The charge distributions of the **HF** and **LF** are shown in Fig. 2. For the **LF**, which is plotted on the right side, the charge distribution for the COMD (teal lines) and AMD (purple lines) results matches the experimental results (black lines) fairly well. The COMD and AMD results with GEMINI (dotted colored lines) underpredicts the charge of the larger Z_L fragments. However, applying GEMINI does not significantly

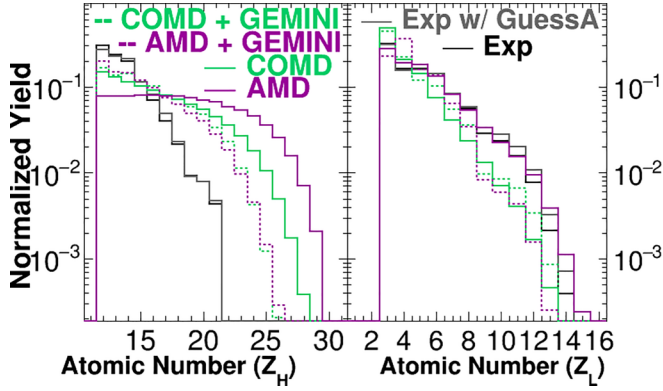


FIG. 2. Charge distribution of the **HF** (left) and **LF** (right). Experimental results are plotted in black, the teal lines are COMD results and the purple lines are the AMD results. The solid lines are the non-GEMINI results and the dotted lines are the GEMINI results. The experimental Z_L distribution is well reproduced by the simulations. The experimental Z_H distribution shows a cut off at $Z_H = 21$ due to the isotopic limitations of the NIMROD array. This cut off is not implemented in the simulated data.

change the shape of the distribution. In the case of the **HF**, both simulations with and without GEMINI overpredict the average charge of the **HF** relative to the experimental results. This effect is due to the isotopic requirement of the **HF**. The charge distribution falls off quickly after $Z_H = 16$ since the number of Si-Si-CsI stacks in NIMROD with isotopic identification for $Z > 16$ decreases significantly with only one Si-Si-CsI stack having isotopic resolution up through $Z = 21$. Although the simulations do not match the distribution well for larger Z , only the results for $Z_H \leq 19$ will be presented in this analysis.

To determine the origin of the **HF** and **LF**, the velocity distributions of the fragments was examined. No requirement on the charge of each **HF** or **LF**, outside of the previously discussed range was applied due to the low statistics in each data set. The velocity distributions are shown in Fig. 3, where the red lines represent the v_H and the blue lines represent the v_L . The solid lines show the experimental distribution, the dashed lines show the AMD results, and the dotted line shows the COMD results. Both the COMD and AMD simulation distributions include the GEMINI afterburner. The dotted, black line indicates the midvelocity ($0.13c$) and the beam velocity ($0.27c$).

The average velocity of both the **HF** and **LF** is peaked above the midvelocity, indicating the majority of fragments decay from the PLF*. The ordering of $\langle v_H \rangle > \langle v_L \rangle$ shows a strong preference for the PLF* to decay on a short timescale with the **HF** having a velocity near the beam velocity. The velocity of the **LF** is consistent with originating from the neck region, indicating dynamical decay where the fragments decay promptly along the axis of separation and consistent with previous experimental results [4,6,16]. The simulated data have a lower average velocity relative to the experimental results for both v_H and v_L with the exception of the COMD v_H . This indicates the collision parameters are causing the fragments to overinteract.

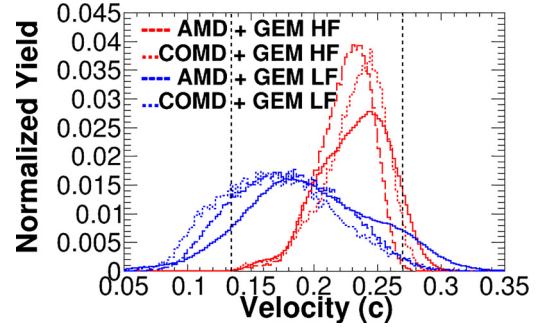


FIG. 3. Simulated **HF** and **LF** velocity distributions after GEMINI is applied compared to the experimental distributions. The red lines represent the **HF** and the blue lines represent the **LF**. The solid lines are the experimental distributions, the dashed lines are the AMD distributions and the dotted lines are the COMD distributions. The left and right black, dotted lines correspond to the midvelocity and beam velocity, respectively. The $\langle v_H \rangle$ and the $\langle v_L \rangle$ are both above midvelocity. An ordering is observed where $\langle v_H \rangle > \langle v_L \rangle$.

IV. ANGULAR DISTRIBUTIONS

Angular distributions may also provide insight into the reaction dynamics. The angle of rotation is defined as the dot product between the center of mass velocity ($\vec{v}_{c.m.}$) and relative velocity ($\vec{v}_{REL} = \vec{v}_H - \vec{v}_L$) of the **HF** and **LF** as seen in Eq. (1):

$$\alpha = a \cos \left(\frac{\vec{v}_{c.m.} \cdot \vec{v}_{REL}}{||\vec{v}_{c.m.}|| ||\vec{v}_{REL}||} \right). \quad (1)$$

Figure 4 shows the angular distribution for the experimental and simulated results. The colors are consistent with Figs. 1 and 2, where the black line is experimental, teal is COMD and purple is AMD. The solid teal and purple lines show the COMD and AMD without the GEMINI afterburner results, respectively, and the dotted, colored lines show the results with GEMINI. A large enhancement in the yield is seen at $\cos(\alpha) = 1$ for all cases shown, indicating a preference for

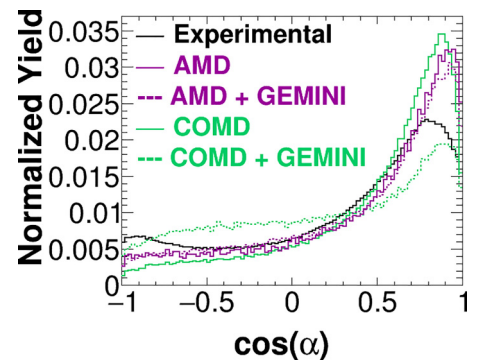


FIG. 4. Cosine α distribution for the experimental and simulated results. The experimental results are shown in black. The COMD are plotted in teal and the AMD results are plotted in purple. The solid lines are results without GEMINI and the dotted lines are the results with GEMINI. A large enhancement of the yield is seen at $\cos(\alpha) = 1$ consistent with dynamical decay. The background present for $\cos(\alpha) < 0$ indicated the presence of statistical decay.

decay of the **HF** forward relative to the **LF**. The yield falls off quickly as $\cos(\alpha)$ decreases reaching a minimum around $\cos(\alpha) = -0.3$. A flattening in the distribution is seen for $-1 < \cos(\alpha) < -0.3$.

The large enhancement at $\cos(\alpha) = 1$ is due to the large presence of dynamical decay. As mentioned previously, a PLF* that is highly elongated and deformed will most likely break apart on a very short timescale along the PLF-TLF axis of separation. The longer the PLF* remains in contact, the longer the PLF* rotates around its center of mass, resulting in a smaller $\cos(\alpha)$. The dynamical contribution is dominant at small angles of rotation, eventually becoming negligible for $\cos(\alpha) < -0.3$, where statistical decay becomes the most dominant mechanism. Interestingly, there is a lack of yield at the $\cos(\alpha) = -1$ edge of the distribution relative to the experimental results, suggesting the simulated total angular momentum is lower. The total angular momentum for both COMD and AMD is peaked at $8\text{--}10 \hbar$ for the **HF** and $2\text{--}5 \hbar$ for the **LF**. Direct comparison to the experimental data is not possible due to a lack of well characterized total angular momenta at Fermi energies.

The two decay mechanisms can be further explored by examining the angular distribution from the COMD and AMD data with and without GEMINI de-excitation. The simulation times are fairly short (300 fm/c for AMD and 1000 fm/c for COMD), allowing the projectile and target to interact and separate. Since dynamical decay occurs rapidly after the PLF-TLF break up, the majority of the fragments that break apart into an **HF** and a **LF** before GEMINI de-excitation are produced dynamically. Throughout the remainder of the analysis, these events will be referred to as coming from a *different* source. For events where the PLF* remains intact at the end of the COMD simulation and before GEMINI, the **HF** and **LF** are produced through statistical GEMINI de-excitation. These reactions will be referred to as coming from the *same* source.

Figure 5 shows the contribution of the COMD and AMD distribution after the GEMINI afterburner was applied. The teal and purple distributions show the COMD and AMD distribution, respectively, shown in Fig. 4. The blue distribution is the different-source distribution, and the orange distribution is the same-source distribution. The different-source distribution is peaked at approximately $\cos(\alpha) = 1$ and falls off exponentially. A small background is seen at $\cos(\alpha) < 0$, which is likely due to the small statistical decay contribution. The same-source distribution is symmetric around $\cos(\alpha) = 0$, which is consistent with isotropic or statistical decay. Quantitatively, the contribution from the same source is 69% for COMD and 25% for AMD simulations. A direct comparison to the experimental distribution is not feasible. However, using a method consistent with the method used in Ref. [9], the statistical contribution is estimated to be 57%.

The larger statistical contribution in the COMD distribution is due to the clusterization parameters. Nucleons are defined to be in the same fragment if the center of mass of the nucleons is within 2.76 fm of each other. A large number of events still have fragments within the clusterization radius at the end of the COMD simulation and are therefore defined as one fragment. Since GEMINI assumes a spherical initial source, the deformation of the PLF* is not preserved resulting in the

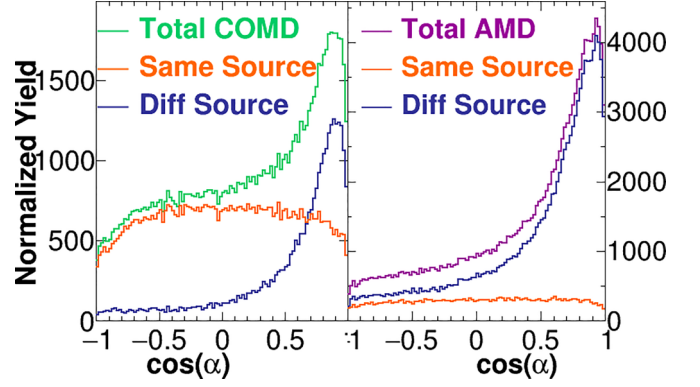


FIG. 5. Cosine α distribution after GEMINI is applied broken down based on the source of the PLF* decay. The teal and purple distributions are the total COMD and AMD distributions shown in Fig. 4. The navy distribution corresponds to “different” sources, in which an **HF** and **LF** are present at the end of the COMD or AMD simulation. The distribution is peaked around $\cos(\alpha) = 1$ and falls exponentially consistent with most dynamical decay. The orange distribution is the “same” source cases where the PLF* remains intact at the end of the COMD or AMD simulations, and GEMINI breaks the fragment into the **HF** and **LF**. The distribution is isotropic consistent with statistical decay.

HF and **LF** being emitted isotropically. Due to this loss of information, all subsequent results from COMD or AMD with GEMINI will focus solely on different-source events.

V. EXAMINING AND QUANTIFYING NZ COMPOSITION AS A FUNCTION OF TIME

The composition of the **HF** and **LF** was calculated using the equation $\Delta = \frac{(N-Z)}{A}$. Due to the limited statistics, the average composition for each Z_H was calculated with no requirement on the charge of the **LF**, and vice versa for each Z_L for the COMD simulations. For the AMD simulations, all **HF** and **LF** were added together. The composition was examined for each of the three density dependence parameters for the asymmetry energy (soft, stiff, and superstiff) simulated in the COMD data. Two density dependence parameters were used in the AMD simulations (soft and stiff). The composition for both simulations was calculated before and after the GEMINI afterburner was applied.

Starting with the COMD simulations, the compositions of the **HF** and **LF** for each interaction were plotted as a function of α . The **HF** and **LF** were sorted by Z_H and Z_L , respectively. To highlight the features present across all interactions, the results for the soft interaction are shown in the top four panels in Fig. 6. The panels on the left show the composition of the **LF** versus α , and the panels on the right show the composition of the **HF** versus α . The top row corresponds to the results without GEMINI, and the middle row corresponds to the results with GEMINI. The bottom two panels correspond to the experimental results from Refs. [8,9] gated on the charge of the Z_L (left) or Z_H (right). The coloring in the left panels is consistent and shows the composition for $3 \leq Z_L \leq 9$, which represent the Z_L range analyzed in Refs. [8,9]. Likewise, the coloring in the right panels is the same and shows the composition

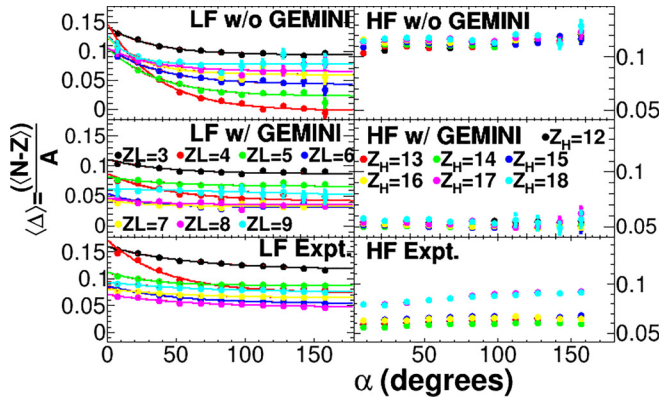


FIG. 6. COMD $\langle \Delta \rangle$ vs α results for the soft interaction and experiment. The left column corresponds to the results gated on the charge of the **LF**, and the right column corresponds to the results gated on the charge of the **HF**. The top row corresponds to the results without GEMINI and the middle row corresponds to the results after GEMINI is applied. The bottom row is the experimental results. Each color in the top panels represents a different Z_L ranging between $3 \leq Z_L \leq 9$, consistent with the experimental range examined in Ref. [8,9] and shown in the bottom, left plot. The color range in the bottom panels corresponds to $12 \leq Z_H \leq 18$. The exponential decrease in the Z_L is seen, consistent with the experimental results. The **HF** results do not show the exponential trend observed in the experimental data.

for $12 \leq Z_H \leq 18$, also consistent with the range analyzed in Refs. [8,9]. The colored lines are the exponential fits for the corresponding colored points. The exponential fits will be discussed subsequently.

For the **LF** without GEMINI (top, left), the composition for each Z_L starts off relatively neutron-rich before exponentially decreasing as α increases, eventually plateauing around $\alpha \simeq 100^\circ$. A clustering in the initial composition ($\Delta_{\text{init},L}$) of the simulated data is seen, which is not present in the experimental data shown in the bottom panel of Fig. 6. This clustering is believed to be an artifact of the molecular dynamics code. The odd-even effect from the experimental data is not seen in the COMD simulations where instead the asymptotic values are sorted from smallest to largest atomic number.

After GEMINI is applied, the exponentially decreasing trend in the Δ_L remains. The $\Delta_{\text{init},L}$ with GEMINI is lower than the $\Delta_{\text{init},L}$ without GEMINI. The corresponding asymptotic values are also lower relative to the non-GEMINI data. The odd-even effect in the final composition ($\Delta_{L,\text{final}}$) is present, consistent with experimental trends shown in the bottom row of Fig. 6. The extent of the equilibration ($|\Delta_{\text{final},L} - \Delta_{\text{init},L}|$) is reduced in the GEMINI results.

Next, the composition of the **HF** is shown in the right panels in Fig. 6. For the events without GEMINI de-excitation, a slight increase in composition as a function of α is observed. However, the increase in composition is not exponential and the shape of the evolution is not consistent with the experimental results plotted in the bottom, right panel of Fig. 6.

When GEMINI is applied, the initial composition of **HF** is approximately half as neutron-rich, which is more consistent with the experimental initial compositions. The distribution is

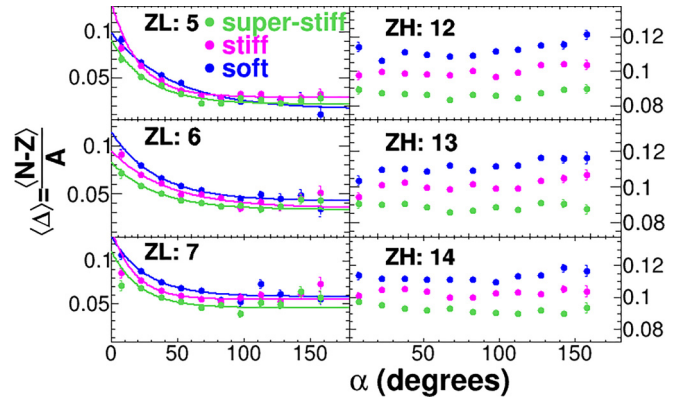


FIG. 7. $\langle \Delta \rangle$ vs α for select Z_L and Z_H . Each panel shows all three COMD interactions. The blue points correspond to the soft interaction, the pink points correspond to the stiff interaction, and the green points correspond to the superstiff interaction. The left panels show the results for $5 \leq Z_L \leq 7$, and the right panels show the results for $12 \leq Z_H \leq 14$. An ordering is seen for both Z_L and Z_H , where the soft interaction is the most neutron-rich followed by the stiff and then superstiff interactions.

fairly flat with a slight overall decrease seen in the composition between $60^\circ < \alpha < 120^\circ$. The statistics above $\alpha = 120^\circ$ are too poor to qualitatively examine the evolution of the composition.

To compare the results across each interaction, Fig. 7 shows Δ_L and Δ_H as a function of α for three select Z_L and Z_H values. The results do not include GEMINI in order to focus solely on the reaction dynamics present in COMD. The left panels correspond to $5 \leq Z_L \leq 7$, from top to bottom, and the right panels correspond to $12 \leq Z_H \leq 14$. The Z_H and Z_L values include those highlighted in Ref. [8]. Each color corresponds to a different interaction where the blue points represents the soft interaction, the pink points are the stiff one, and the green points are the superstiff one.

For the Z_L , all three interactions show the same general trend where the composition exponentially evolves as a function of α . The values for the composition throughout the distribution are very similar, with the largest difference between points corresponding to $\Delta_L = 0.03$ (≈ 0.5 neutrons). An ordering is seen where the initial composition for the soft interaction (blue points) is most neutron rich, followed by the stiff (pink) and superstiff (green) interaction, respectively. The ordering effect is seen throughout all Z_L , with the exception of $Z_L = 5$ for the soft interaction. The change in $\langle \Delta_{\text{init},L} \rangle$ is due to the dynamics during the nucleon drift phase of the projectile and target interaction. The difference between the asymmetry energy at and below the saturation density is the largest for the stiff interactions. Therefore, the potential barrier for the enhanced neutron flow is higher for the stiffer interactions, which causes less neutrons to flow to the neck region relative to the soft interaction.

For the **HF**, the overall trends for each interaction are not as consistent with each other as for Δ_L . For the soft interaction, an overall increase between the initial and final composition is seen. For the stiff interaction, the increase, while present, is suppressed and not present for the super-stiff interaction.

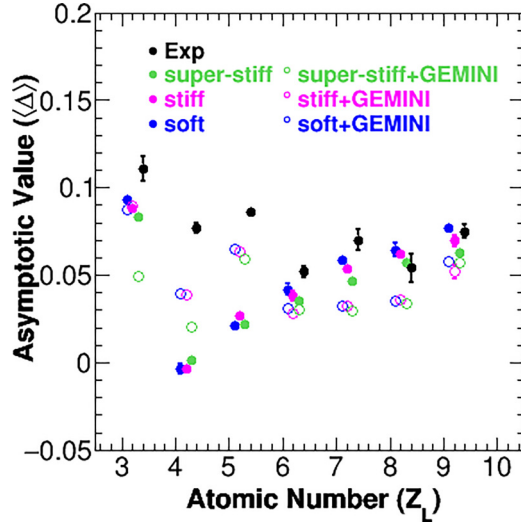


FIG. 8. The asymptotic values for the COMD and experimental **LF** results. The blue points are the soft interaction, the pink points are the stiff interaction, and the green points are the superstiff interaction. The black points are the experimental results. The closed points are the non-GEMINI results, and the open points are the GEMINI results. The non-GEMINI results show an overall increase in the neutron-richness as the charge increases. The only exception is $Z_L = 3, 4$ due to the presence of unstable proton-rich fragments. The GEMINI results show the odd-even effects observed in the experimental results. In the majority of cases, the neutron composition of the simulation results was underestimated relative to the experimental ones.

Similar to the Δ_L results, the neutron-richness increases as the interaction gets softer. While this initial neutron-richness is well understood for the Δ_L based on the form of the asymmetry energy, one would expect a change in the ordering of the Δ_H . In a bimodal system, the excess neutrons seen in the neck (**LF**) region should originate from the PLF (**HF**), making the $\Delta_{\text{init},H}$ most neutron poor for the soft interaction.

To quantify the difference in the compositions between interactions, each $\langle \Delta_L \rangle$ vs α distribution was fit with an exponential of the form seen in Eq. (2). The a is the asymptotic value, b is the pre-exponential factor, and c is the rate constant in degrees. The exponential was fit between $20^\circ < \alpha < 120^\circ$, which is consistent with the experimental data. The simulation results were binned more coarsely than the experimental ones due to lower statistics. The Δ_H data was not fit due to the lack of exponential nature in the **HF** results.

$$\langle \Delta \rangle = a \exp(-c\alpha). \quad (2)$$

The results for the asymptotic values are seen in Fig. 8. The black points correspond to the experimental values and the coloring for the three COMD interactions is consistent with Fig. 7. The solid points represent the values without GEMINI, and the open points are the values with GEMINI.

Overall, the asymptotic compositions of each Z_L with and without GEMINI underpredict the composition relative to the experimental values. The only exception is $Z_L = 8, 9$ for the results without GEMINI. In the experimental results, an odd-even effect is seen with the even-charged fragments having a smaller $\langle \Delta_L \rangle$ value relative to their neighbors. The odd-

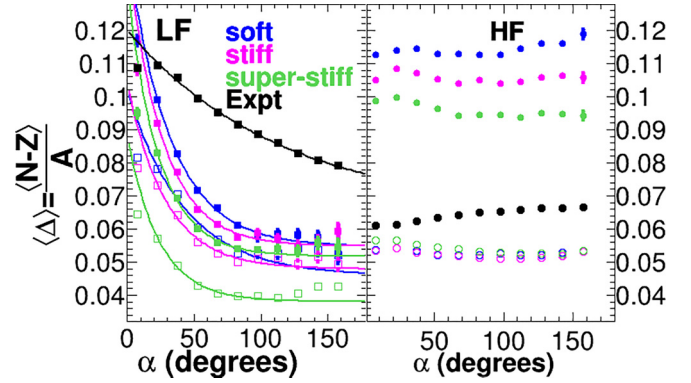


FIG. 9. COMD $\langle \Delta \rangle$ vs α of the **LF** (left) and **HF** (right) for the combined **HF** and **LF** results. The blue points correspond to the COMD soft interaction, the pink points correspond to the COMD stiff interaction, and the green points correspond to the COMD superstiff interaction. The black points are the experimental ones. The respectively colored lines are the exponential fits. The closed circles are the values without GEMINI, and the open circles are the value with GEMINI. The results show an exponential trend for the **LF** results for all interactions with and without GEMINI, consistent with the experimental results. The neutron composition of the **LF** is underpredicted by the COMD simulations. For the **HF**, the non-GEMINI results overpredict the neutron-richness of the fragments, whereas the GEMINI results underpredict the neutron-richness.

even effect is preserved for the GEMINI results. Examining the results without GEMINI can give insight into the effects of secondary decay on the final compositions. The results point to GEMINI over-de-exciting the **LF** relative to the experimental results. In the results without GEMINI, the final composition increases linearly between $Z_L = 5-9$. In the case of $Z_L = 3, 4$, the composition does not follow the same trend due to the production of nonstable isotopes. $Z_L = 4, A_L = 8$, and $Z_L = 3, A_L = 4, 5$ is converted to the corresponding combinations of p, d, α particles after the COMD simulation has finished, increasing the asymptotic value.

To best compare the COMD and AMD simulations, all Z_H and Z_L were combined to view the total **HF** and **LF** compositions over α . The results for COMD and AMD are shown in Figs. 9 and 10, respectively.

For both figures, the left panels corresponds to the composition of the **LF**, and right panels correspond to the **HF**. The results without GEMINI are plotted in closed squares or circles, and results with GEMINI are plotted with open squares or circles. The coloring in Fig. 9 is consistent with the coloring in Fig. 6. For Fig. 10, the yellow points correspond to the soft interaction, and the orange-red points correspond to the stiff interaction.

The COMD results for the combined **HF** and **LF** without GEMINI are consistent with the previously discussed trends, where Δ_L exponentially decreases and Δ_H is fairly flat, increasing slightly for the soft interaction. The ordering from most to least neutron rich of soft, stiff and superstiff is still present for **HF** and **LF**. The curvature of the exponential decrease in Δ_L is approximately the same across the three

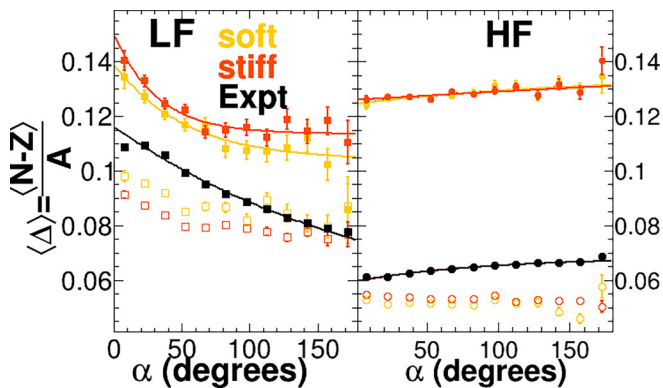


FIG. 10. AMD $\langle \Delta \rangle$ vs α of **LF** (left) and **HF** (right) for the combined **HF** and **LF** results. The yellow points correspond to the AMD soft interaction, the red points correspond to the AMD stiff interaction, and the black points correspond to the experimental ones. The respectively colored lines are the exponential fits. The closed circles are the values without GEMINI, and the open circles are the value with GEMINI. The results show an exponential trend for the **HF** and **LF** results for both of the interactions and the experimental results. The non-GEMINI results overpredict the neutron-richness of the fragments, whereas the GEMINI results underpredict the neutron-richness.

interactions, indicating the rate of change in the composition is similar for each interaction.

Interestingly, this is not true for the Δ_L results after GEMINI was applied. The curvature of the superstiff interaction is greatest with the distribution approaching the asymptotic value at $\alpha \approx 80^\circ$. The stiff interaction has less curvature, approaching its asymptotic value at $\alpha \approx 120^\circ$. The asymptotic value is yet to be approached at $\alpha = 180^\circ$ for the soft interaction.

Another difference between the Δ_L with and without GEMINI is the initial composition. $\Delta_{\text{init},L}$ without GEMINI was $\approx 25\%$ greater than $\Delta_{\text{init},L}$ with GEMINI. While the overall composition throughout the distribution was greater for the results without GEMINI, the composition for the stiff and superstiff interactions started to merge towards each other. The asymptotic values differ by only $\Delta_L \approx 0.09$ (0.2 neutrons). The most stark difference in composition is seen for the soft interaction, potentially due to the low Z_L values dominating the isotopic distribution.

When the **LF** composition results are compared to the experimental ones, a stark deviation is seen. Unlike the COMD data, the experimental rate of change is much slower where the final composition at $\alpha = 180^\circ$ is far from the asymptotic value. The deviation from the experimental data is due to the combination of the Z_H and Z_L , which will be discussed in further detail at the end of the section when quantitatively comparing rate constants.

For the **HF**, the application of GEMINI did not significantly change the shape of the distribution. GEMINI caused the compositions to collapse onto each other at $\Delta_H \approx 0.55$. A change in the ordering of the points is observed where the super-stiff interaction is the most neutron rich followed by the stiff and the soft interactions, respectively. The change is most likely

due to the stability of the initial compositions of **HF** after COMD, since the average angular momentum and excitation energy of the **HF** are consistent for the three interactions. The average initial composition for the soft interaction corresponds to an excess of ≈ 3 –5 neutrons, which is on the higher side of the valley of stability. Due to the large neutron excess, GEMINI is more likely to over-de-excite the fragments to achieve stability, resulting in less neutron-rich compositions for the more neutron-rich inputs.

The COMD results without GEMINI presented in this work can be contrasted to previous COMD simulation results from Stiefel *et al.* [17]. In both analyses, the composition of the **LF** for $Z_L = 4$ shows a decrease in the composition as a function of α . However, a direct comparison of the shape of the distribution cannot be made due to the difference in binning between analyses. In both analyses, an ordering is seen where the softest interaction is the most neutron rich. The greatest difference arises when comparing the **HF** distributions. The **HF** distributions in Ref. [17] show an equivalent increase in the composition as α increases for all three interactions. An opposite ordering is seen where the soft interaction is the least neutron rich. These results are in contrast with the results observed in this work. Sources of the difference may include the time-step at which the data was analyzed and the experimental filter through which the simulation was passed.

For the AMD simulations, the **LF** results without GEMINI show the composition of the **LF** for both interactions starts off relatively neutron rich and evolves exponentially to be less neutron rich as α increases consistent with the experimental trends [8,9]. One notable difference between the two interactions is the composition of the **LF**. For the stiff interaction, the composition starts off more neutron rich, which is in contradiction to the enhanced neutron flow in the neck region due to the potential energy barrier. While the two values start to merge around $\alpha = 80^\circ$, the asymptotic composition of the stiff interaction is much larger for the stiff interaction. This greater curvature observed for the stiff interaction indicates a larger rate constant.

The results after the GEMINI afterburner is applied show an overall decrease in the composition as a function of α relative to the results without GEMINI. The composition decreases fairly linearly for $\alpha \leq 60^\circ$. For $60^\circ < \alpha < 120^\circ$, $\langle \Delta_L \rangle$, the value starts to plateau before decreasing again. While the de-excited results mirror the non-de-excited results, the exponential decay is not as pronounced in the results with the de-excitation.

When focusing on the **HF** results without GEMINI, an overall increase in the composition of the **HF** is seen as a function of α . The increase in the composition for both interactions is exponential in nature. The initial composition of the **HF** is more neutron-poor for the soft interaction consistent with a greater neutron contribution to the neck region from the PLF during the momentum dampening phase. In both cases, the curvature is less pronounced as the experimental data, indicating a slower neutron exchange process.

The GEMINI results show a flat distribution across the entire α range. The overall composition for the **HF** is lower than the results without GEMINI. The lack of the increasing trend

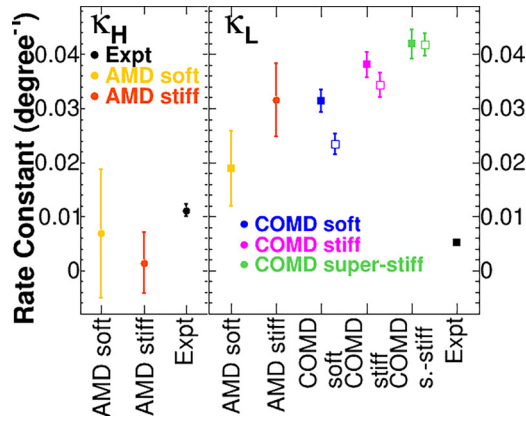


FIG. 11. Rate constant (κ) of the **HF** (left) and **LF** (right) for the combined **HF** and **LF** results. The coloring is consistent with Figs. 9 and 10. Only κ_H and κ_L are shown, where the exponential fit converged. The κ_H shows agreement between the AMD soft interaction and the experimental results, while the κ_H for the stiff interaction underpredicts the rate constant. For κ_L , the AMD soft interaction reproduces the experimental κ_L well within error bars. The AMD stiff interaction and the COMD results with and without GEMINI overpredict κ_L .

is most likely due to GEMINI over-de-exciting the fragments, washing out this effect.

A similar trend was observed in the Piantelli *et al.* [18] analysis. In the case of $Z_L = 5$, AMD simulations with GEMINI were able to reproduce the decrease in the composition as a function of α observed in the experimental data. The exponential increase in the **HF** composition was not observed in the AMD data with GEMINI, consistent with the results presented in this work. However, it is important to note the exponential trend was also not observed in the experimental data shown in Ref. [18].

To quantitatively compare the simulated results for **HF** and **LF** to the experimental ones and each other, the rate constants were plotted in Fig. 11. The coloring for all panels is consistent with the coloring in Figs. 9 and 10. The left panel shows the rate constant for **HF** (k_H), and the right panel shows the results for the **LF** rate constant (k_L). Only the results were shown for systems where an exponential fit converged. For the k_L results for COMD, two values were plotted: Results without GEMINI in closed points and results with GEMINI in open points. The GEMINI points are offset slightly to allow better comparison of the data. The y-axis range is the same for both panels.

The **HF** exponential fits only converged for the AMD data without GEMINI and the experimental results. Both the AMD soft and stiff results underpredict the experimental value. In the case on the soft interaction, the value is consistent within error bars with the experimental value.

For the **LF**, the fits converged for the AMD results without GEMINI, COMD results with and without GEMINI, and the experimental results. Unlike the **HF** results, the rate constant for the AMD stiff interaction is greater than the rate constant for the AMD soft interaction. Only the AMD soft results are consistent within error bars with the experimental results. For the

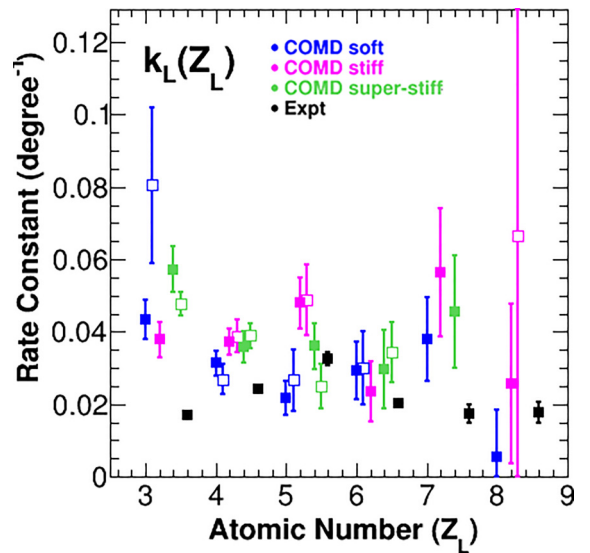


FIG. 12. Rate constant as a function of Z_L ($k_L(Z_L)$) for the three COMD interactions with and without GEMINI and the experimental results. The blue points correspond to the soft interaction, the pink points correspond to the stiff interaction, and the green points correspond to the superstiff interaction. The closed points are the non-GEMINI results and the open points are the GEMINI results. The black points are the experimental values. The majority of the simulated points are greater than the experimental ones.

COMD results, an ordering is seen for both the results without GEMINI (closed squares) and with GEMINI (open squares), where the soft interaction has the lowest rate constant, followed by the stiff and the superstiff ones, respectively. For the superstiff results, the rate constant was approximately equal for the calculations with and without GEMINI. A shift is seen for the soft and stiff case, where the GEMINI rate constant is smaller than the non-GEMINI one. The greatest effect is seen for the soft interaction. Both the COMD results with and without GEMINI have rate constants significantly greater than the experimental ones.

The comparison between the experimental and simulated data can be further explored by looking at the effect of charge sorting on the rate constant. Figure 12 shows the rate constant for each Z_L [$k_L(Z_L)$] with no condition on the charge of the corresponding **HF**. The coloring and use of open and closed points is consistent with previous COMD figures. Only results where the exponential fit converged are shown. The values are offset based on whether or not the results include GEMINI and the stiffness of the interaction used. Overall, the rate constants for all three interactions across a given Z_L are constant within error bars. Greater deviation is seen for larger Z_L due to statistical limitations. In the majority of cases, the simulated rate constants are overestimated relative to the experimental results.

However, unlike the results seen in the left panel of Fig. 11, the experimental and simulation results in Fig. 12 are more similar. Figure 13 shows the effect of charge-sorting the data on the average rate constant. In the left panel, the first six points show the rate constant for the **LF** (κ_L) when all **HF** and **LF** fragments were combined, followed by the average

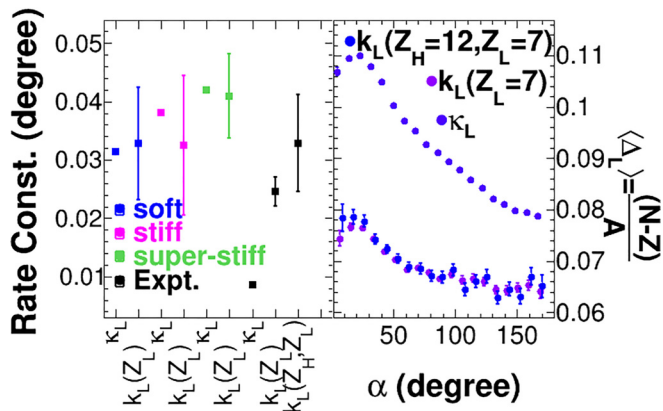


FIG. 13. The left panel shows the **LF** rate constant for the combined **HF** and **LF** system (κ_L) and the average **LF** rate constant for the system sorted by Z_L [$k_L(Z_L)$]. The blue, pink, and green results correspond to the soft, stiff, and superstiff interaction input for the COMD simulations. The black points are the experimental values, which also include the averaged **LF** rate constant for the system sorted by Z_H, Z_L pairings. Results show agreement between the κ_L and $k_L(Z_L)$ for each interaction. A large increase in the rate constant is shown in the experimental results as the sorting requirements become more stringent. The right panel shows example Δ_L vs α experimental distributions for the combined system (darker purple), system gated on $Z_L = 7$ (lighter purple), and system gated on $Z_H = 12, Z_L = 7$ (blue).

rate constant for the **LF** [$k_L(Z_L)$] gated on Z_L for each COMD stiffness interaction. The last three points correspond to the rate constant extracted for the experimental data when all fragments were combined together (κ_L), the averaged value for k_L for a given Z_L , and lastly, the averaged value for k_L for all Z_H, Z_L pairings shown in Ref. [9]. All average values were calculated using weighted averages. Focusing first on the COMD results, the rate constants κ_L and $k_L(Z_L)$ for each interaction are consistent within error bars. Deviation between the κ_L and $k_L(Z_L)$ values is most likely due to the statistics when calculating the weighted average.

The greatest effect is seen in the experimental results. For the case where no restrictions were made on the charge of the **HF** or **LF**, the rate constant is the lowest, indicating the rate of change is the slowest. When gating solely on the charge of the **LF**, the average rate constant is approximately doubled, and approximately tripled when also gating on the charge of the partner fragment.

The effect is further visible when looking at the right panel of Fig. 13. The darker purple points correspond to the combined results. The lighter purple points are Δ_L vs α values for $Z_L = 7$ and no cut on the charge of Z_H , and the blue points are the corresponding values for $Z_H = 12, Z_L = 7$. The difference in the evolution of the composition is due to the mixed yield contribution from various sources. If the yield distribution as a function of α was equivalent for all Z_H, Z_L pairings, the rate constant should be consistent regardless of the selection on Z_L and/or Z_H . Instead, the yield for smaller Z_H and Z_L values is significantly greater. In addition, as discussed in Refs. [8,9], the peak of the α distribution moves closer to $\alpha = 0^\circ$ for larger

$Z_H + Z_L$ and $Z_H - Z_L$. As the **HF** and **LF** system becomes more charge-symmetric, a greater yield is seen at $\alpha > 120^\circ$.

Therefore, the Δ_L value across the α distribution starts similar to the more neutron-rich Δ_L vs α distributions seen in Refs. [8,9]. The larger relative contribution from the large Z_L values decreases the $\langle \Delta_L \rangle$ at smaller and larger α . The flattening of the distribution results in a smaller rate constant. The same effect to a lesser extent is seen in the Δ_L vs α distribution for the results gated solely on $Z_L = 7$ as seen in Fig. 13. The resulting average rate constant is intermediate relative to the combined and Z_H, Z_L paired ones.

VI. CONCLUSION

The overall trends in the AMD and COMD results point towards a smaller L value reproducing the experimental trends better. In the case of the AMD data, both the soft and stiff interactions reproduced the experimental trends seen for **LF** and **HF** well. The rate of change in the composition of both **LF** and **HF** for the smaller L -value interaction were more consistent with the experimental data.

For the COMD results, the exponential increase in the **LF** composition was seen for all three interactions. An ordering is seen for the results with and without GEMINI, where the soft interaction is the smallest, followed by the stiff interaction, and then the superstiff one. Yet, all of the interactions have a rate constant greater than the experimental one. For the **HF**, an increase in the composition is seen for the soft interaction, which is minimized for the stiff interaction and not present for the superstiff interaction. The trend is not exponential or consistent with the experimental results.

However, greater agreement in the rate constants for the COMD simulations is seen when the **LF** fragments were sorted by Z_L . While the experimental average rate constant is still lower than the simulated ones, the value is approximately twice as large as the results for the combined **HF, LF** experimental result. Furthermore, upon comparing the weighted average of the experimental results when sorting solely on the charge of the **LF** versus sorting on the charge of both the **HF** and **LF**, another increase in the average rate constant was seen. The value increased from $k_L(Z_L) \simeq 0.2$ to $k_L(Z_H, Z_L) \simeq 0.3$. Therefore, the most accurate view of the evolution of the composition of the binary decay mechanism can be examined when sorting on both the Z_H and Z_L .

Further examination of the dynamics observed in the simulation as well as a larger simulation data set may give further insight into the evolution of the composition of the **HF** and **LF** and, therefore, the functional form of the density dependence of the asymmetry energy.

ACKNOWLEDGMENTS

We would like to thank the staff at the Cyclotron Institute at Texas A&M University for providing the excellent quality of beams. We would like to thank Z. Kohley for data collection and calibration. We would further like to thank the computer group at the Cyclotron Institute at Texas A&M University for maintaining the supercomputer array. This work was supported by the Robert A. Welch Foundation through

Grant No. A-1266, the Department of Energy through Grant No. DE-FG02-93ER40773, and the National Nuclear Security Administration under Award No. DE-NA0003841. We would

like to thank Dr. Ono for use of the AMD code, Dr. Papa for use of the COMD code, and Dr. Charity for the use of the GEMINI code.

-
- [1] V. Baran, M. Colonna, and M. Di Toro, Neck fragmentation reaction mechanism, *Nucl. Phys. A* **730**, 329 (2004).
- [2] C. J. Horowitz, E. F. Brown, Y. Kim, W. G. Lynch, R. Michaels, A. Ono, J. Piekarewicz, M. B. Tsang, and H. H. Wolter, A way forward in the study of the symmetry energy: Experiment, theory, and observation, *J. Phys. G: Nucl. Part. Phys.* **41**, 093001 (2014).
- [3] D. Thériault, J. Gauthier, F. Grenier, F. Moisan, C. St-Pierre, R. Roy, B. Davin, S. Hudan, T. Paduszynski, R. T. de Souza, E. Bell, J. Garey, J. Iglío, A. L. Keksis, S. Parketon, C. Richers, D. V. Shetty, S. N. Soisson, G. A. Souliotis, B. C. Stein *et al.*, Neutron-to-proton ratios of quasiprojectile and midrapidity emission in the $^{64}\text{Zn} + ^{64}\text{Zn}$ reaction at 45 MeV/nucleon, *Phys. Rev. C* **74**, 051602(R) (2006).
- [4] F. Bocage, J. Colin, M. Louvel, G. Auger, Ch. O. Bacri, N. Bellaize, B. Borderie, R. Bougault, R. Brou, P. Buchet, J. L. Charvet, A. Chbihi, D. Cussol, R. Dayras, N. De Cesare, A. Demeyer, D. Doré, D. Durand, J. D. Frankland, E. Galichet *et al.*, Dynamical effects in nuclear collisions in the Fermi energy range: Aligned breakup of heavy projectiles, *Nucl. Phys. A* **676**, 391 (2000).
- [5] B. Davin, R. Alfaro, H. Xu, L. Beaulieu, Y. Larochelle, T. Lefort, R. Yanez, S. Hudan, A. L. Caraley, R. T. de Souza, T. X. Liu, X. D. Liu, W. G. Lynch, R. Shomin, W. P. Tan, M. B. Tsang, A. Vander Molen, A. Wagner, H. F. Xi, C. K. Gelbke, R. J. Charity *et al.*, Fragment production in noncentral collisions of intermediate-energy heavy ions, *Phys. Rev. C* **65**, 064614 (2002).
- [6] J. Colin, D. Cussol, J. Normand, N. Bellaize, R. Bougault, A. M. Buta, D. Durand, O. Lopez, L. Manduci, J. Marie, J. C. Steckmeyer, B. Tamain, A. Van Lauwe, E. Vient, B. Borderie, F. Lavaud, N. Le Neindre, P. Pawłowski, E. Plagnol, M. F. Rivet, B. Bouriquet *et al.*, Dynamical effects in multifragmentation at intermediate energies, *Phys. Rev. C* **67**, 064603 (2003).
- [7] E. De Filippo, A. Pagano, P. Russotto, F. Amorini, A. Anzalone, L. Auditore, V. Baran, I. Berceanu, B. Borderie, R. Bougault, M. Bruno, T. Cap, G. Cardella, S. Cavallaro, M. B. Chatterjee, A. Chbihi, M. Colonna, M. D'Agostino, R. Dayras, M. Di Toro, J. Frankland *et al.*, Correlations between emission timescale of fragments and isospin dynamics in $^{124}\text{Sn} + ^{64}\text{Ni}$ and $^{112}\text{Sn} + ^{58}\text{Ni}$ reactions at 35a mev, *Phys. Rev. C* **86**, 014610 (2012).
- [8] A. Jedelev, A. B. McIntosh, K. Hagel, M. Huang, L. Heilborn, Z. Kohley, L. W. May, E. McCleskey, M. Youngs, A. Zarrella, and S. J. Yennello, Characterizing Neutron-Proton Equilibration in Nuclear Reactions with Subzeptosecond Resolution, *Phys. Rev. Lett.* **118**, 062501 (2017).
- [9] A. Rodriguez Manso, A. B. McIntosh, A. Jedelev, K. Hagel, L. Heilborn, Z. Kohley, L. W. May, A. Zarrella, and S. J. Yennello, Detailed characterization of neutron-proton equilibration in dynamically deformed nuclear systems, *Phys. Rev. C* **95**, 044604 (2017).
- [10] S. Wuenschel, K. Hagel, R. Wada, J. B. Natowitz, S. J. Yennello, Z. Kohley, C. Bottosso, L. W. May, W. B. Smith, D. V. Shetty, B. C. Stein, S. N. Soisson, and G. Prete, Nimrod-isis, a versatile tool for studying the isotopic degree of freedom in heavy ion collisions, *Nucl. Instrum. Methods Phys. Res. A* **604**, 578 (2009).
- [11] Z. Kohley, Transverse collective flow and emission order of mid-rapidity fragments in Fermi-energy heavy ion collisions, Ph.D. thesis, Texas A&M University, 2010.
- [12] M. Papa, T. Maruyama, and A. Bonasera, Constrained molecular dynamics approach to fermionic systems, *Phys. Rev. C* **64**, 024612 (2001).
- [13] A. Ono and H. Horiuchi, Antisymmetrized molecular dynamics for heavy ion collisions, *Prog. Part. Nucl. Phys.* **53**, 501 (2004).
- [14] B. Harvey, M. Youngs, A. McIntosh, A. Jedelev, A. Abbott, J. Gauthier, K. Hagel, A. Hannaman, K. Kriebel, Y.-W. Lui, L. A. McIntosh, A. Rodriguez Manso, M. Sorensen, Z. Tobin, R. Wada, A. Zarrella, and S. J. Yennello, Correlation between time and angular alignment in molecular dynamics simulations of heavy ion collisions, *Phys. Rev. C* **102**, 064625 (2020).
- [15] R. J. Charity, n - z distributions of secondary fragments and the evaporation attractor line, *Phys. Rev. C* **58**, 1073 (1998).
- [16] S. Hudan, A. B. McIntosh, R. T. de Souza, S. Bianchin, J. Black, A. Chbihi, M. Famiano, M. O. Frégeau, J. Gauthier, D. Mercier, J. Moisan, C. J. Metelko, R. Roy, C. Schwarz, W. Trautmann, and R. Yanez, Tracking saddle-to-scission dynamics using n/z in projectile breakup reactions, *Phys. Rev. C* **86**, 021603(R) (2012).
- [17] K. Stiefel, Z. Kohley, R. T. deSouza, S. Hudan, and K. Hammerton, Symmetry energy dependence of long-timescale isospin transport, *Phys. Rev. C* **90**, 061605(R) (2014).
- [18] S. Piantelli, G. Casini, A. Ono, G. Poggi, G. Pastore, S. Barlini, A. Boiano, E. Bonnet, B. Borderie, R. Bougault, M. Bruno, A. Buccola, A. Camaiani, A. Chbihi, M. Cicerchia, M. Cinausero, M. D'Agostino, M. Degerlier, J. A. Dueñas, Q. Fable *et al.*, Dynamical fission of the quasiprojectile and isospin equilibration for the system $^{80}\text{Kr} + ^{48}\text{Ca}$ at 35 MeV/nucleon, *Phys. Rev. C* **101**, 034613 (2020).